





## Review

# Microwave-Assisted Fabrication of High Energy Density Binary Metal Sulfides for Enhanced Performance in Battery Applications

Kenna L. Salvatore <sup>1</sup>, Justin Fang <sup>1</sup>, Christopher R. Tang <sup>2,3</sup>, Esther S. Takeuchi <sup>1,2,3,4</sup>, Amy C. Marschilok <sup>1,2,3,4</sup> , Kenneth J. Takeuchi <sup>1,2,3,4,\*</sup>  and Stanislaus S. Wong <sup>1,\*</sup>

<sup>1</sup> Department of Chemistry, State University of New York at Stony Brook, Stony Brook, NY 11794-3400, USA

<sup>2</sup> Department of Materials Science and Chemical Engineering, State University of New York at Stony Brook, Stony Brook, NY 11794-3400, USA

<sup>3</sup> Institute for Energy Sustainability and Equity, State University of New York at Stony Brook, Stony Brook, NY 11794-3400, USA

<sup>4</sup> Interdisciplinary Science Department, Brookhaven National Laboratory, Upton, NY 11973-5000, USA

\* Correspondence: kenneth.takeuchi.1@stonybrook.edu (K.J.T.); stanislaus.wong@stonybrook.edu (S.S.W.)

**Abstract:** Nanomaterials have found use in a number of relevant energy applications. In particular, nanoscale motifs of binary metal sulfides can function as conversion materials, similar to that of analogous metal oxides, nitrides, or phosphides, and are characterized by their high theoretical capacity and correspondingly low cost. This review focuses on structure–composition–property relationships of specific relevance to battery applications, emanating from systematic attempts to either (1) vary and alter the dimension of nanoscale architectures or (2) introduce conductive carbon-based entities, such as carbon nanotubes and graphene-derived species. In this study, we will primarily concern ourselves with probing metal sulfide nanostructures generated by a microwave-mediated synthetic approach, which we have explored extensively in recent years. This particular fabrication protocol represents a relatively facile, flexible, and effective means with which to simultaneously control both chemical composition and physical morphology within these systems to tailor them for energy storage applications.

**Keywords:** binary metal sulfides; microwave chemistry; synthesis; battery applications



**Citation:** Salvatore, K.L.; Fang, J.; Tang, C.R.; Takeuchi, E.S.; Marschilok, A.C.; Takeuchi, K.J.; Wong, S.S. Microwave-Assisted Fabrication of High Energy Density Binary Metal Sulfides for Enhanced Performance in Battery Applications. *Nanomaterials* **2023**, *13*, 1599. <https://doi.org/10.3390/nano13101599>

Academic Editors: Andreu Cabot and Carlos Miguel Costa

Received: 13 March 2023

Revised: 7 April 2023

Accepted: 5 May 2023

Published: 10 May 2023



**Copyright:** © 2023 by the authors. Licensee MDPI, Basel, Switzerland. This article is an open access article distributed under the terms and conditions of the Creative Commons Attribution (CC BY) license (<https://creativecommons.org/licenses/by/4.0/>).

## 1. Introduction

Binary semiconducting metal sulfides ( $M_xS_y$ ) possess novel optical, electrical, and chemical properties, and have been considered for a multitude of different applications. Specifically, they have been developed as building blocks for photovoltaic devices, including dye-sensitized cells, all-inorganic nanoparticle solar cells, and hybrid nanocrystal-polymer composite solar cells, in addition to lasers, waveguides, and other optoelectronic devices [1–4]. Moreover, they have found usage as either supercapacitors or catalysts for the hydrogen and oxygen evolution reactions [5–7]. In addition, they have been investigated for biomedical applications [8–10], including but not limited to biosensors and photothermal therapy.

In the context of this Review, metal sulfides frequently have been assessed for their viability as components of batteries. Specifically, they can function as conversion materials, similar to that of analogous metal oxides, nitrides, or phosphides, and are characterized by their high theoretical capacity and correspondingly low cost [11,12]. In particular, binary metal sulfides are attractive candidates as electrodes for battery applications, because of their advantageous attributes for increasing latent charge and ion mobility through (i) the exposure of reactive surface areas, (ii) a favorable reduction in ion diffusion distances, and (iii) an enhancement in cyclability. Furthermore, the utilization of metal sulfides as

battery-active materials is particularly tantalizing not only due to the possibility of both anionic and cationic redox activity, where the transition metal cation can be reduced, but also because of the inclusion and functionality associated with the sulfur moiety [13,14]. Accessing the electrochemical reactivity of both species necessitates employing a broad voltage range; however, the benefit of this is the possibility of very high capacities. The use of a wide voltage window renders the selection of the current collector critical. For lithium batteries, low voltages can only be accessed using a copper current collector to avoid the formation of lithium-aluminum alloys with an aluminum foil current collector [15]. However, to access high voltages, the use of copper is not possible, due to the possibility of copper oxidation. A solution that has been employed in the past has been to use a carbon matrix as the current collector in order to avoid the reactivity that is inherent to the metal foil current collectors [16]. By comparison with more commonly used oxides, metal sulfides benefit from (a) a wider palette of possible achievable redox chemistries, (b) superior conductivities, and (c) improved reversibilities [17]. Conversely, sulfides are hindered from realizing their full theoretical potential for battery applications by limitations such as poor cycling retention due to issues ascribable in part to volume expansion and low conductivity.

One promising approach towards mitigating these deficiencies is to produce these materials as their nanoscale analogs [18]. As is well known, nanomaterials can possess properties which differ significantly from and can be better than those of the corresponding bulk due to the vast increase in surface area-to-volume ratios and associated surface-induced effects at this scale. Specifically, the advantages of creating nanoscale motifs include but are not limited to (a) an increase in the number of active sites, (b) shorter distances associated with a more rapid and effective electron and ion transport, (c) the potential for spatial confinement and control of electron and ion movement in either one or more dimensions, and (d) a greater resistance to volume change (and hence, an improved cycle stability).

Indeed, the community has found that, while shrinking down metal sulfides to nanoscale formulations is a helpful generalizable strategy, the approach is complicated by factors such as (1) dimensionality and (2) the presence of conductive additives, which also play key roles in terms of impacting the inherent electrochemical performance of these materials. We define the nature of dimensionality in terms of the conventionally accepted sense of enabling spatial confinement along orthogonal planes of as-prepared structures to the nanoscale regime. Hence, representative examples of zero-dimensional (0D), one-dimensional (1D), two-dimensional (2D), and three-dimensional (3D) nanomaterials include quantum dots, nanowires, nanosheets, and sea-urchin assemblies, respectively.

From the literature, it is known that 0D materials tend to maintain not only a greater structural and cycling stability but also a reduced volume expansion compared to bulk. By comparison, 1D structures exhibit not only an increased surface area but also shortened distances for both electron and Li-ion transport. In addition, 2D materials are characterized by large surface areas, thereby resulting in an increased number of exposed active sites, shortened Li-ion diffusion distances, and superior structural stability [11]. However, despite the clear benefits associated with 0D, 1D, and 2D motifs, the performance of these materials can often be hindered by aggregation effects, which manifest themselves in observables such as a decrease in cycling [19]. Hence, 3D architectures, which ironically often consist of agglomerations of individual 0D, 1D, and/or 2D components [11], have been found in some cases to combine and incorporate the best attributes of all of these constituent units. Specifically, 3D motifs often display a high overall surface area for reactivity, especially when compared with either 0D or 1D analogs, with implications for (a) the presence of a plethora of active surface sites; (b) diminished Li diffusion distances; (c) an enhanced structural stability; and (d) a favorable reduction in not only overall aggregation of the material but also undesirable re-stacking of lower-dimensional building blocks, such as nanosheets [11]. As such, 3D nanoscale structures frequently demonstrate better structural stability, specific capacity, and rate performance metrics as compared with 0D, 1D, and 2D

analogs, respectively, due not only to their increased reactive surface areas but also to their ability to moderate volume expansion effects during relevant redox reactions [20–23].

With respect to the addition of conductive additives, we note that although a number of other equally valid and significant approaches (including but not limited to either the insertion of molecular and elemental dopants or the addition of self-healing polymers [24,25]) also exist, herein we focus our discussion on the introduction of discrete carbon-based materials, such as 1D carbon nanotubes (CNTs), 2D graphene, graphene oxide (GO), reduced graphene oxide (rGO), and liquid-exfoliated graphene (LEGr). It has been noted that these materials, in combination with either metal sulfides or oxides, lead to unique hierarchical assemblies, characterized by a greater stability, a notably better conductivity, and the capability for accommodating volume changes during cycling [26]. As an example, analysis of a mixture of multi-walled carbon nanotubes (MWNTs) coupled with metal oxides revealed notable improvements in electrochemical activity for battery applications as compared with pristine and unfunctionalized metal oxides alone [27]. Furthermore, other reports have emphasized the benefits of introducing carbon additives, such as rGO [28,29] and graphene [30,31], for appreciably boosting cycling stability and capacity.

With the ultimate goal of enhancing conductivity and reducing the extent of volume change due to electrochemical reactions within binary metal sulfides, this review therefore centers on structure–composition–property relationships, emanating from deliberative attempts to either (1) vary and alter the dimension of nanoscale architectures or (2) introduce conductive carbon-based entities. It should be noted that many distinctive synthesis techniques [32–34], such as hydrothermal, solid-state, and solvothermal-inspired reactions, have been previously reported for these nanoscale metal sulfide motifs. Nevertheless, as compared with these other methods, rapid and uniform heating (made possible using microwave irradiation in particular) can yield advantages, such as a short reaction time, a facility of synthesis, and a consistency of the resulting product in terms of size, shape, and composition.

Therefore, in this Review, we will primarily concern ourselves with metal sulfide nanostructures generated by a microwave-mediated synthetic approach [35,36], which we have explored extensively in recent years. To highlight the significance of this body of work, in Table 1, we summarize data from the literature pertaining to specific capacities measured over multiple cycles of diverse metal sulfide electrode nanomaterials, synthesized using microwave-assisted processes. The metal sulfide nanoparticles we have considered in this Review, namely copper sulfide, iron sulfide, molybdenum sulfide, and vanadium sulfide, can be broadly divided into two general categories, based on their crystal structure, i.e., layered versus non-layered. In this context, we consider and correlate some of the more important defining parameters of these systems, such as theoretical capacity, cost, toxicity, and morphology, as well as the facility of their synthesis.

**Table 1.** Sustained specific capacities measured over multiple cycles of metal sulfide electrode nanomaterials, synthesized through microwave-assisted processes. Unless otherwise noted, capacities were measured in half-cell configurations with the appropriate metal (Li, Na, Mg) as the counter/reference electrode.

Material	Ion Type	Capacity (mA h g <sup>−1</sup> )	Lifespan	Reference
CuS nanosheets	Mg	135	200 cycles @ 200 mA g <sup>−1</sup>	[37]
CuS nanosheet superstructures	Na	347	1000 cycles @ 5 A g <sup>−1</sup>	[38]
CuS nanosphere/CNT composites	Li	437–569	250 cycles @ 400 mA g <sup>−1</sup>	[39]
CuS nanoflower/rGO composites	Li	390	200 cycles @ 500 mA g <sup>−1</sup>	[40]
CuS nanosheet/rGO composites	Na	345	450 cycles @ 1 A g <sup>−1</sup>	[41]

Table 1. Cont.

Material	Ion Type	Capacity (mA h g <sup>-1</sup> )	Lifespan	Reference
CuS nanoparticles on graphene	Li	348	1000 cycles @ 2 A g <sup>-1</sup>	[26]
ZnS nanoparticle/rGO composites	Na	481	50 cycles @ 100 mA g <sup>-1</sup>	[42]
Co <sub>9</sub> S <sub>8</sub> /rGO composites	Na	346	30 cycles @ 100 mA g <sup>-1</sup>	[43]
In <sub>2</sub> S <sub>3</sub> nanoflowers on graphene	Li	657	40 cycles @ 70 mA g <sup>-1</sup>	[44]
In <sub>2</sub> S <sub>3</sub> nanoparticles on graphene	Li	522	100 cycles @ 700 mA g <sup>-1</sup>	[44]
Ni <sub>3</sub> S <sub>2</sub> and Ni <sub>7</sub> S <sub>6</sub> nanoparticle/rGO composites	Na	392	50 cycles @ 100 mA g <sup>-1</sup>	[45]
MoS <sub>2</sub> nanoparticles	Li	544	500 cycles @ 5 A g <sup>-1</sup>	[46]
MoS <sub>2</sub> nanosheet/CNT-sulfur composites	Li-S	694	200 cycles @ 835 mA g <sup>-1</sup>	[47]
SnS <sub>2</sub> nanosheet/LEGr composites	Li	664	200 cycles @ 300 mA g <sup>-1</sup>	[48]
WS <sub>2</sub> /graphene composites	Li	714	100 cycles @ 300 mA g <sup>-1</sup>	[49]
WS <sub>2</sub> /graphene composites	Li	534	450 cycles @ 1 A g <sup>-1</sup>	[49]
VS <sub>4</sub> /rGO composites	Li	1144	50 cycles @ 100 mA g <sup>-1</sup>	[50]
VS <sub>4</sub> hollow nanospheres	Na	1130	1000 cycles @ 2 A g <sup>-1</sup>	[51]
Cu@MoS <sub>2</sub> core/shell nanowires	Li	571	250 cycles @ 500 mA g <sup>-1</sup>	[52]
Mo <sub>0.5</sub> W <sub>0.5</sub> S <sub>2</sub> alloy nanoflowers	Li	272	400 cycles @ 1 A g <sup>-1</sup>	[53]
CuS <sub>0.96</sub> Te <sub>0.04</sub> nanosheets	Mg	115	200 cycles @ 500 mA g <sup>-1</sup>	[54]

## 2. Advantages and Disadvantages of Microwave-Assisted Methods

The obvious question is: why microwave-based chemistry [55]? Microwave-assisted methods to produce metal sulfides represent the use of a potentially environmentally sustainable means with which to fabricate nanomaterials using shortened reaction times with uniform heating across the reaction medium, while simultaneously maintaining control over a large number of reaction parameters in order to enable the facile production of respectable quantities of pure and homogeneous products with high yields. Many wet chemical processes are unable to readily satisfy all of these criteria at once, associated with ensuring sample purity. Moreover, whereas reaction variables, such as time, temperature, and precursors, can be carefully tuned and tailored, as with most other synthesis protocols including but not limited to hydrothermal and solvothermal techniques, microwave-derived procedures [35,36] offer a much broader parameter space with which to tweak and optimize product formation with comparative ease, including but not limited to power, pressure, and solvent selection.

In particular, solvent identity is a crucial choice, because the solvent must not only be miscible with the precursor solute molecules but also be capable of absorbing microwave energy, as measured by its tangent factor ( $\delta$ ) [56]. As an example, in a previous paper by this group, we found that VS<sub>4</sub> nanoflowers could be reliably generated over a range of sizes in high quantities and yields simply by changing the polarity of the solvent, which in turn influenced the resulting reaction kinetics and thereby impacted the dimension and morphology of the final product [18].

Prior reports have found that the choice of the synthesis method used to create testable samples (such as metal sulfides in particular) has a significant impact, with clear implications for the resulting electrochemical performance. As an illustrative example comparing the relative benefits of using materials derived from microwave-assisted versus hydrothermal methods, several studies have analyzed this issue in the context of optoelectronic applications [36], supercapacitors [57], electrocatalytic reactions such as the hydrogen evolution reaction (HER) [58], and lithium-ion batteries (LIBs) [59–61]. In particular, with respect to the performance of ZnCo<sub>2</sub>O<sub>4</sub> flower-like materials [8] generated using both



synthesis techniques, the sample fabricated via microwave irradiation exhibited an enhanced cycling performance after 45 cycles of  $1411 \text{ mA h g}^{-1}$  as compared with the much lower value of  $217 \text{ mA h g}^{-1}$  for its hydrothermally produced analogue. One plausible explanation for the observed difference is that the microwave-initiated material in question was characterized by smaller crystallite sizes. As we will subsequently explore, similar types of behavior have been observed with respect to the use of distinctive classes of metal sulfides incorporated within lithium-ion, sodium-ion, magnesium-ion, and lithium-sulfur batteries as either the anode or the cathode.

For the sake of completeness, we should note that one possible disadvantage of microwave-assisted methods based on anecdotal evidence in our lab is that, depending on the targeted system, sample size, shape, and crystallinity are not necessarily homogeneous and uniform within isolated samples produced by this technique, and as such, are more difficult to simultaneously control. Moreover, depending on the configuration of the microwave reactor, the maximum volume of a reaction vessel may be limited, thereby potentially hindering scale-up of the method. As a corollary issue [62], the fact that microwave systems cannot easily be incorporated into existing engineering scaffolds for the fabrication of large-scale materials needed for battery production is a significant disadvantage, since the replacement of current similar conventional systems would require a good deal of investment. Additionally, in many cases involving the use of microwave irradiation in facilitating chemical transformations, the true origins of the overall microwave enhancement and heating effect are either uncertain or poorly understood, which does not help in enabling the widespread implementation and acceptance of this technology.

### 3. Non-Layered Binary Sulfides (Copper, Zinc, Cobalt, Indium, and Iron)

We will first consider binary metal sulfides characterized by non-layered crystal structures, i.e., typically sulfides incorporating late-transition and post-transition metals. Many types of these metal sulfides generated via microwave-assisted synthesis have been utilized for battery applications. One common example is green covellite copper sulfide (CuS), which possesses an elevated electronic conductivity ( $10^{-3} \text{ S cm}^{-1}$ ), a favorable theoretical capacity ( $560 \text{ mA h g}^{-1}$ ), and a correspondingly large voltage hysteresis profile—of relevance for their use as LIB anodes [63,64]. Not surprisingly, due to its comparatively low cost and high abundance, CuS has been tested in magnesium-ion [37,65,66], lithium-ion [26,39,40,67,68], and sodium-ion [38,41] battery applications. In terms of dimensionality, CuS spheres [39], nanotubes [66], nanosheets [37,38,65,68], nanodiscs [69], and nanoflowers [40] have been generated using microwave-mediated processes.

In a typical reaction, copper chloride (copper source) and thioacetamide (sulfur source) were added to a mixed solvent containing water and ethanol and irradiated at 300 W for 30 min to yield nanosheets measuring roughly 200 nm in diameter (Figure 1A) [37]. These materials exhibited promise as Mg-ion cathodes, demonstrating not only an enhanced reversible discharge capacity of  $300 \text{ mA h g}^{-1}$  at  $20 \text{ mA g}^{-1}$  but also an exceptional cycling stability of  $135 \text{ mA h g}^{-1}$  at  $200 \text{ mA g}^{-1}$  over 200 cycles (Figure 1B). The performance of these motifs can be attributed to their 3D hierarchical structure, in which the constituent component nanosheets maintain a large surface area that is exposed for interaction with the electrolyte while also providing sufficient space for expansion and contraction, which is associated with ion intercalation and removal. Furthermore, as another example, camellia-like nanosheet superstructures of CuS have been produced via the combination of PVP, copper chloride, and sodium thiosulfate through a microwave-assisted reaction [38]. The resulting catalyst served as an excellent anode material in sodium-ion batteries, exhibiting a stable capacity of  $347.1 \text{ mA h g}^{-1}$ , even after 1000 cycles at  $5.0 \text{ A g}^{-1}$  [38].

Reflecting an alternate approach, CuS materials have also been combined together with conductive carbon additives, such as CNTs [39,67], reduced graphene oxide (rGO) [40,41], and graphene [26], in order to boost both cycling stability and overall conductivity versus control samples consisting of CuS alone; the incorporation of reduced graphene oxide in particular led to noticeable benefits. We elaborate on these as-produced structures as fol-

lows. A CuS/CNT composite was generated via an in situ microwave-assisted reaction, in which CuS spheres were grown onto the underlying CNT backbone; indeed, the nucleation of CuS on the CNTs was enabled by the fact that as a material, the CNTs preferentially heated faster than the solvent itself under microwave irradiation conditions [39].

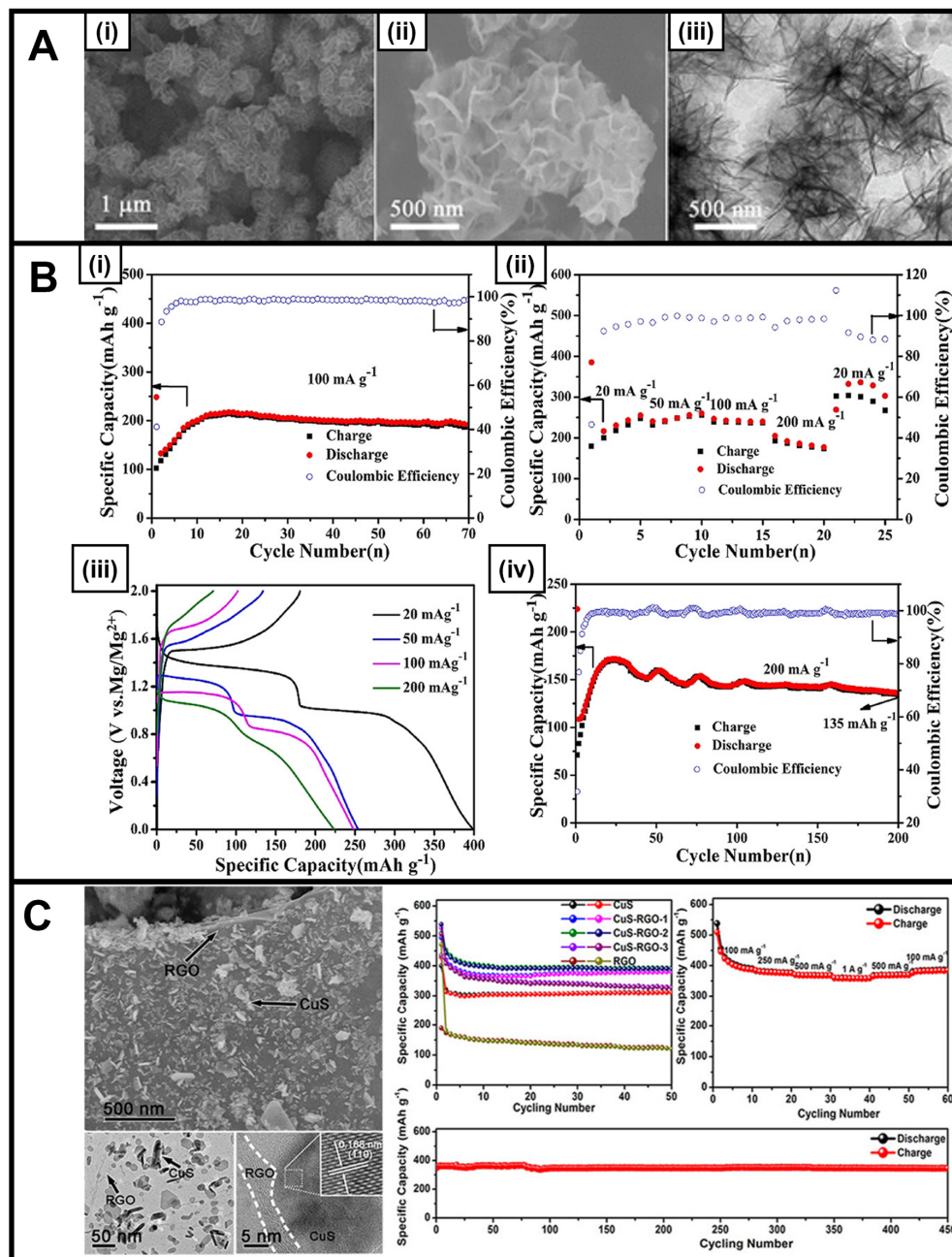


**Figure 1.** (A) (i,ii) SEM images and (iii) TEM image of the hierarchical CuS nanosheets, produced via a ‘microwave heating’ method [37]. (B) (i) Capacity and CE of the CuS electrode at 100 mA g<sup>-1</sup>, (ii) rate capabilities of the CuS electrode with various current densities from 20 to 200 mA g<sup>-1</sup>, (iii) discharge and charge profiles at different current densities, and (iv) long-term cycling of the CuS electrode at 200 mA g<sup>-1</sup> [37]. (C) FESEM and TEM images of CuS-rGO-2 at low and high magnifications and cycling performance of CuS, CuS-rGO-1, CuS-rGO-2, CuS-rGO-3, and rGO at a current density of 100 mA g<sup>-1</sup>; rate performance of CuS-rGO-2; and long cycling performance of CuS-rGO-2 at 1 A g<sup>-1</sup> [41]. Panels (A,B) have been adapted with permission from ref. [37]. Copyright 2019 American Chemical Society. Panel (C) has been adapted with permission from ref. [41]. Copyright 2017 American Chemical Society.

Moreover, at different levels of CNT incorporation, the microwave-generated CuS/CNT composite performed noticeably better as an anode in a Li-ion battery than identical analogs derived from ball milling processing, an observation which can be ascribed to an improved integration between CuS and CNTs within microwave-generated samples. The electrochemical testing was conducted using an electrode prepared on a Cu foil positioned within a coin cell versus a lithium counter electrode using 1 M lithium bis(trifluoromethanesulfonyl)imide within a 1,3-dioxolane and dimethyl ether electrolyte. As such, the cycling tests were conducted in lithium metal half-cells. Specifically, in these microwave-derived composites, excellent stability was recorded after 450 cycles at  $400 \text{ mA h g}^{-1}$ , with measured capacities ranging from 437 to  $569 \text{ mA h g}^{-1}$  as a function of increasing CNT content.

A complementary CuS-rGO composite consisting of CuS nanosheets and rGO was tested as an anode replacement for Na-ion storage. It yielded a measured specific capacity of  $392.9 \text{ mA h g}^{-1}$  after 50 cycles at a current density of  $100 \text{ mA h g}^{-1}$  coupled with a high initial Coulombic efficiency of 94% (Figure 1C), in addition to a sustained specific capacity of  $345 \text{ mA h g}^{-1}$  noted after 450 cycles at a current density of  $1 \text{ A g}^{-1}$  [41]. The effects of the electrolyte were also tested within this system, with demonstrably improved performance measured in an ether-based solvent due to its ability to suppress polysulfide intermediates. A final example of a CuS/graphene composite was created under in situ reaction conditions involving the use of sodium thiosulfate as the sulfur precursor and copper chloride as the copper precursor in a mixture, which was subjected to a power cycling algorithm; the as-produced CuS nanoparticles were deposited onto underlying graphene sheets. The resulting composite gave rise to an improved reversible capacity of  $348 \text{ mA h g}^{-1}$ , which was maintained after 1000 cycles at a current density of  $2.0 \text{ A g}^{-1}$ . It was determined that the CuS component had benefited from enhanced Li-ion transfer and reduced contact resistance, as a result of its attachment to adjoining graphene sheets [26].

Other studies have explored additional, analogous materials, such as zinc sulfide (ZnS) [42], indium sulfide ( $\text{In}_2\text{S}_3$ ) [44], nickel sulfide [45], and cobalt sulfide ( $\text{Co}_9\text{S}_8$ ) [43], as well as iron sulfide ( $\text{FeS}_2$  and  $\text{Fe}_3\text{S}_4$ ) for sodium-ion [42,43,45] and lithium-ion battery [44,70] applications. It is worth noting that ZnS is known for a favorable combination of non-toxicity, comparatively low cost, and relatively high theoretical capacity in LIB ( $962.3 \text{ mA h g}^{-1}$ ) [71]. As an example, ZnS nanoparticles were made via a microwave-assisted method in less than 15 min in the presence of varying amounts of GO [42]. By optimizing the amount of GO within the sample, the ensuing ZnS-rGO electrode delivered a high specific capacity of  $481 \text{ mA h g}^{-1}$ , measured at  $100 \text{ mA g}^{-1}$  after 50 cycles for sodium-ion battery anodes, denoting observations ascribable in part to the greater surface area and better electronic conductivity associated with the addition of rGO [42].

$\text{Co}_9\text{S}_8$  materials possess an intrinsically high capability, when used as anode materials. To reinforce the significance and advantages of graphene addition, composites incorporating quasi-spherical motifs of microwave-derived  $\text{Co}_9\text{S}_8$  and rGO delivered improved activity within SIB anodes. Specifically, a high reversible capacity of  $426.2 \text{ mA h g}^{-1}$  at a current density of  $100 \text{ mA g}^{-1}$  was measured and remained at a relatively high value of  $346.3 \text{ mA h g}^{-1}$  even after 30 cycles, a finding which was attributable in part to the presence of the rGO additive. The presence of this additive reduces the  $\text{Co}_9\text{S}_8$  particle size from 200–400 nm down to  $\sim 20 \text{ nm}$ , buffers volume changes associated with charging and discharging, and increases conductivity [43].

Additionally, while mainly utilized in the context of photocatalysts and solar cells,  $\text{In}_2\text{S}_3$  is attractive for battery applications, because it possesses not only a reasonably sizeable theoretical capacity of  $713 \text{ mA h g}^{-1}$  but also a desirable spinel crystal structure similar to that of high-performing materials such as magnetite and lithium titanate [72]. Not surprisingly,  $\text{In}_2\text{S}_3$  nanoflowers and nanoparticles have been dispersed onto graphene nanosheets to form a sandwich-like hierarchical structure for LIB anodes [44]. As a starting point,  $\text{In}_2\text{S}_3$  nanoflowers were first optimized by controlling parameters, such as temperature and time to construct structures measuring several hundred nanometers in diameter at

140 °C for 20 min upon reaction of indium chloride and thioacetamide precursor reagents with CTAB as the surfactant in water (Figure 2A(i)).

To create the corresponding  $\text{In}_2\text{S}_3$ -graphene composites, an in situ reaction was utilized, in which graphene was introduced into the above mixture prior to microwave irradiation. The as-formed  $\text{In}_2\text{S}_3$ -graphene composites exhibited two unique morphologies, denoted as “ $\text{In}_2\text{S}_3$ -graphene nanoparticle-on-sheet” (Figure 2A(iv)) and “ $\text{In}_2\text{S}_3$ -graphene flower-on-sheet” (Figure 2A(ii)) motifs. Whereas both composites revealed more than 1.5 times the reversible capacities of the pristine control material, the “ $\text{In}_2\text{S}_3$ -graphene nanoparticle-on-sheet” structure, in particular, gave rise to a greater cycle stability at larger currents, an observation most likely ascribed to the higher relative quantities of graphene (whose presence can not only reduce volume change but also improve mechanical stability and conductivity) versus those of the nanoflowers present within the sample (Figure 2A(iii)).

In another example, our group has recently worked on iron sulfides ( $\text{FeS}_2$  and  $\text{Fe}_3\text{S}_4$ ) that can be produced using a microwave-based technique.  $\text{FeS}_2$  typically occurs in two forms, namely pyrite (cubic) and marcasite (orthorhombic). However, few reports have demonstrated the ability to isolate either of these crystallographic phases in large quantities at the nanoscale [73]. Nevertheless, phase control and facet formation are important parameters to consider. For example, based on previous studies, the (111) facet (compared with others) of  $\text{FeS}_2$  was particularly considered to be an attractive and promising candidate for LIB anode applications; however, it is difficult to synthesize, due to its comparatively high-energy formation. Because octahedra signify one of the few shapes in which this facet is predominantly featured and exposed, we recently focused on generating pure pyrite  $\text{FeS}_2$  octahedra using microwave-based chemistry in the absence of either surfactants or corrosive solvent conditions so as to decrease the level of impurities and defects that might have interfered with subsequent electrochemical analyses. As such, we employed a solvent mixture of water and ethylene glycol in the presence of thioacetamide and iron chloride as the sulfur and iron precursor, respectively, to fabricate high-quality octahedra (Figure 2B(i)) using a simpler, much faster, and more efficacious protocol than previous approaches [74].

Modifications to this underlying procedure enabled us to synthesize nanosheets of greigite or  $\text{Fe}_3\text{S}_4$ , another iron sulfide which has had limited testing for battery applications despite possessing a relatively high theoretical capacity of  $725 \text{ mA h g}^{-1}$ , arising in part from the consequences of an  $8e^-$  reversible conversion reaction. Greigite is unusual in that, as a sulfide-based spinel, it retains a similar structure to magnetite. To achieve our synthetic objective, we substituted L-cysteine for the sulfur precursor and optimized the metal-to-sulfur ratio in order to control not only the chemical composition but also the resulting morphology. The driving force for a successful reaction appeared to be the choice of the sulfur precursor, as it could dictate the amount of sulfur-containing species present at any given moment within the reaction medium.

Furthermore, the as-synthesized  $\text{Fe}_3\text{S}_4$  nanosheets were also combined with conductive carbon additives, specifically with MWNTs and graphene, albeit by using an ex situ method. (Figure 2B(ii)). The production of these carbon-based composites fortunately did not introduce either apparent impurities or perceptible changes in the isolated morphology. Cyclic voltammetry of the as-generated samples (Figure 2C) shows that the incorporation of carbon is beneficial to the current produced, with the MWNT-containing material evincing greater current values (Figure 2C(ii)) than either the as-synthesized  $\text{Fe}_3\text{S}_4$  alone (Figure 2C(i)) or the graphene-containing heterostructure (Figure 2C(iii)). This observation thereby confirms the clear advantages of introducing conductive carbon additives in order to create high-performing iron sulfide-based composite motifs.



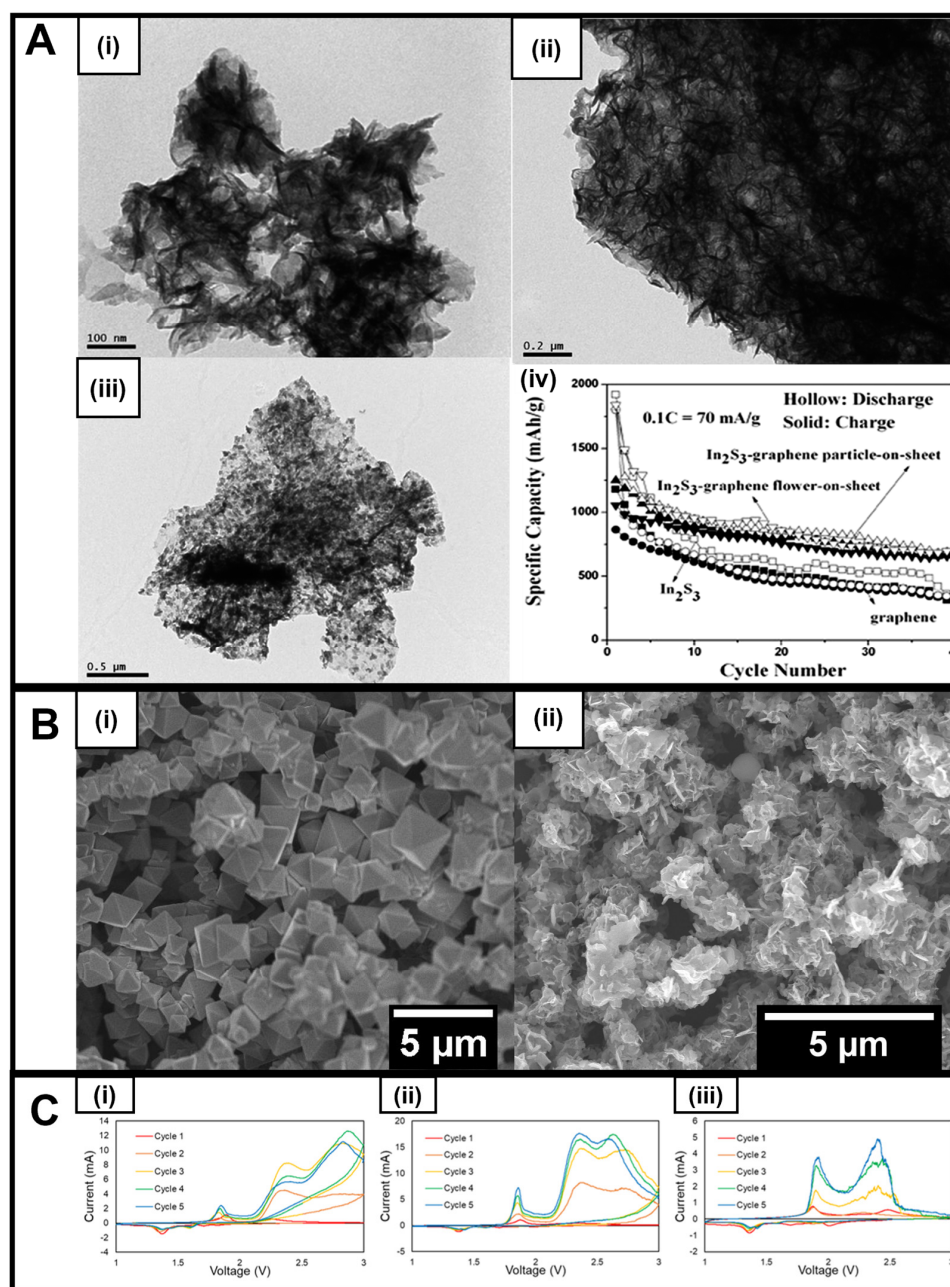


**Figure 2.** (A) (i) TEM image of In<sub>2</sub>S<sub>3</sub> products prepared at 160 °C after 20 min microwave irradiation; (ii) TEM image of In<sub>2</sub>S<sub>3</sub>-graphene composite (flower-on-sheet) [44]; (iii) TEM image of In<sub>2</sub>S<sub>3</sub>-graphene composite (particle-on-sheet); (iv) Cycling performance of In<sub>2</sub>S<sub>3</sub>-graphene composites at 0.1C (70 mA g<sup>−1</sup>) (hollow: discharge, solid: charge) [44]. (B) (i) SEM image of FeS<sub>2</sub> octahedra and (ii) SEM image of Fe<sub>3</sub>S<sub>4</sub> nanosheets. (C) Cyclic voltammetry (CV) results of (i) as-prepared Fe<sub>3</sub>S<sub>4</sub>, along with heterostructures created by incorporation with either (ii) MWNT or (iii) graphene. The CV data, show that the introduction of MWNTs increases measured current values as compared with either Fe<sub>3</sub>S<sub>4</sub> alone or with the analogous graphene-containing heterostructure. Data were collected at a 0.1 mV/s scan rate with voltage limits of 1.0 to 3.0 V. Panel (A) has been reproduced from ref. [44] with permission from the Royal Society of Chemistry.

#### 4. Layered Transition Metal Dichalcogenides (MoS<sub>2</sub>, WS<sub>2</sub>, SnS<sub>2</sub>)

An important subset of metal sulfides encompasses the transition metal dichalcogenides (TMDC) due to their characteristic layered structure, in which transition metal atoms are sandwiched between chalcogenides in such a way to form 2D layers that are



connected to other adjacent layers by weak van der Waals forces. These layers can be used to boost electrochemical performance by taking advantage of the superior ion intercalation potential both within and between the individual, discrete layers [29]. Typical TMDC materials include but are not limited to molybdenum disulfide ( $\text{MoS}_2$ ), tungsten disulfide ( $\text{WS}_2$ ), and tin disulfide ( $\text{SnS}_2$ ).

Molybdenum sulfide is known for its applicability as an anode replacement in lithium-ion [29,31,46], sodium-ion [28,30,31], and lithium-sulfur [47] batteries, evincing both a unique layered structure and favorable electronic properties [28]. Published reports cite the possibility of synthesizing a range of diverse morphologies, such as particles [28,46], nanosheets [30,31,47], and nanocrystals [29]. As previously implied, the choice of the synthesis protocol has an inordinate impact upon the dimensionality and architecture of the resulting product. In this vein, microwave-based methods yielded small 0D nanoparticles ('MW- $\text{MoS}_2$ ') measuring 20 to 30 nm in diameter, whereas analogous hydrothermal techniques produced larger 3D flower-like motifs (HT- $\text{MoS}_2$ ) (Figure 3A) [46]. Upon incorporation into LIB anodes, compared with these flower-like analogs, the smaller MW- $\text{MoS}_2$  nanoparticles demonstrated not only an enhanced initial capacity of  $1199 \text{ mA h g}^{-1}$  but also a high stability during the cycling process, characterized by a Coulombic efficiency of 75% and an exceptional rate capability (Figure 3A) [46]. This unexpected finding was ascribed to the comparatively larger exposed surface area coupled with the substantial pore volume of samples generated during the microwave treatment versus those that had been synthesized hydrothermally.

Separately, 2D  $\text{MoS}_2$  nanosheets produced via a microwave-assisted method in the presence of an ether solvent were probed as cathodes within a binder-free electrode configuration (BFE) for lithium-sulfur battery applications (Figure 3B) [47]. Specifically, these  $\text{MoS}_2$  nanosheets exhibited an excellent capacity of  $694 \text{ mA h/g}_{\text{sulfur}}$  and a specific energy of  $1435 \text{ Wh/kg}_{\text{sulfur}}$  ( $600 \text{ Wh/kg}_{\text{electrode}}$ )—measured at a C/2 rate of  $835 \text{ mA g}^{-1}$  after 200 cycles within a di(propylene glycol) dimethyl ether (DPGDME) electrolyte (Figure 3C) [47]. It should be noted that the use of the BFE configuration gave rise to a significant cycling stability compared with that measured for coated electrodes. Moreover, the addition of a CNT-based network to these  $\text{MoS}_2$  nanosheets led to increased polysulfide trapping, which consequentially improved ion transfer and diffusion.

Microwave-generated tin sulfide ( $\text{SnS}_2$ ), which is known for its inherently high electronic conductivity, has been tested for its applicability in lithium-ion [31,48,75–78] and sodium-ion batteries [31] in the guise of nanoflakes [31,75], intercalated sheets [76], and microflowers [77]. As a layered 2D motif,  $\text{SnS}_2$  gave rise to a relatively high theoretical capacity of  $645 \text{ mA h g}^{-1}$  for LIB applications. The corresponding  $\text{SnS}_2$ -based composites, produced using a microwave-derived technique with tin and sulfur precursors in the presence of liquid exfoliated graphene (LEGr), led to an unusual architecture created by  $\text{SnS}_2$  nanosheets nucleating onto LEGr nanosheets (Figure 4A,B) [48]. This LEGr-based  $\text{SnS}_2$  composite was found to retain a high storage capacity coupled with an enhanced cycling stability of  $664 \text{ mA h g}^{-1}$  after 200 cycles at a  $300 \text{ mA h g}^{-1}$  current density (Figure 4C), with the measured performance attributed to the high conductivity and mechanical stabilization against the volume change provided by LEGr [48].

$\text{WS}_2$  represents another TMDC material, that can form as favorable layered 2D sheets and enable not only superior ion intercalation but also enhanced measured reversibility [29,49]. As such, analogously synthesized LEGr@ $\text{WS}_2$  composites prepared using a microwave-assisted solvothermal method that suppresses the formation of  $\text{WO}_3$  impurities were characterized by a 2D hierarchical structure possessing excellent interfacial contact between the  $\text{WS}_2$  and the LEGr surfaces, denoting a desirable interface for promoting excellent electrochemical performance and cycling stability for LIB anode applications. Moreover, by varying the relative quantities of W and S within these composites, these LEGr@ $\text{WS}_2$  materials displayed not only a reversible capacity of  $714 \text{ mA h g}^{-1}$  after 100 cycles at a current density of  $300 \text{ mA g}^{-1}$  but also a stable capacity of  $534 \text{ mA h g}^{-1}$  after 450 cycles at a high current of  $1 \text{ A g}^{-1}$  [49].

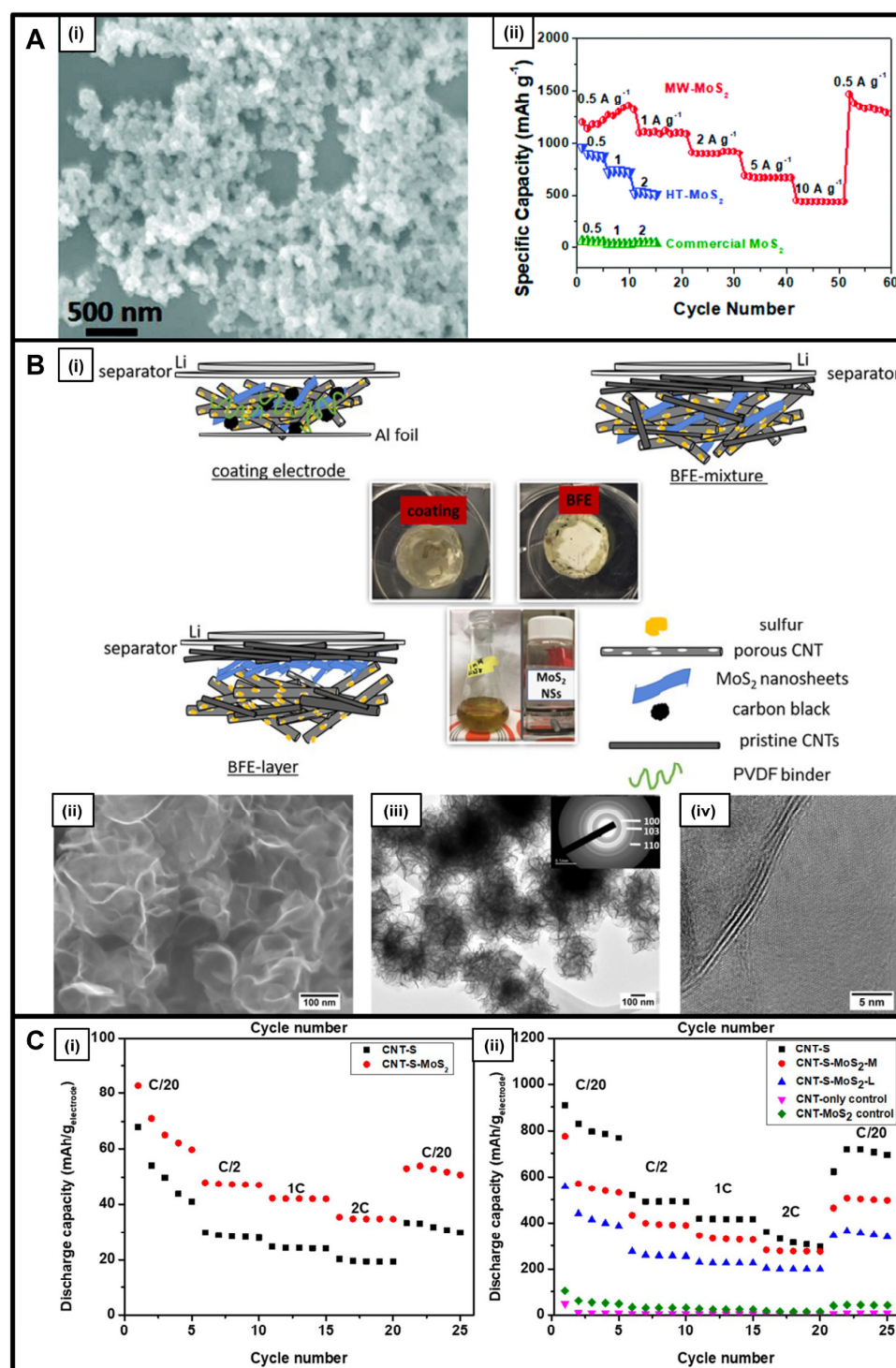


**Figure 3.** (A) (i) SEM image of MW-MoS<sub>2</sub>; (ii) Rate capabilities of MW-MoS<sub>2</sub>, HT-MoS<sub>2</sub> and the commercial MoS<sub>2</sub> at different current densities from 0.5 to 10 A g<sup>-1</sup> [46]. (B) (i) Schematic illustration of coating, BFE-mixture, and BFE-layer cell configurations; (ii) SEM, (iii) TEM, and SAED pattern (inset), (iv) HRTEM of the as-prepared MoS<sub>2</sub> nanosheets [47]. (C) Specific capacity versus cycle number, calculated based on sulfur weight and the total cathode weight for the coating cells (i) and the BFEs (ii) measured at 200, 400, 800, 1600, and 200 mA/g<sub>sulfur</sub> discharge/charge current density [47]. Panel (A) has been reproduced from ref. [46] with permission from the Royal Society of Chemistry. Panels (B,C) have been adapted with permission from ref. [47]. Copyright 2019 American Chemical Society.

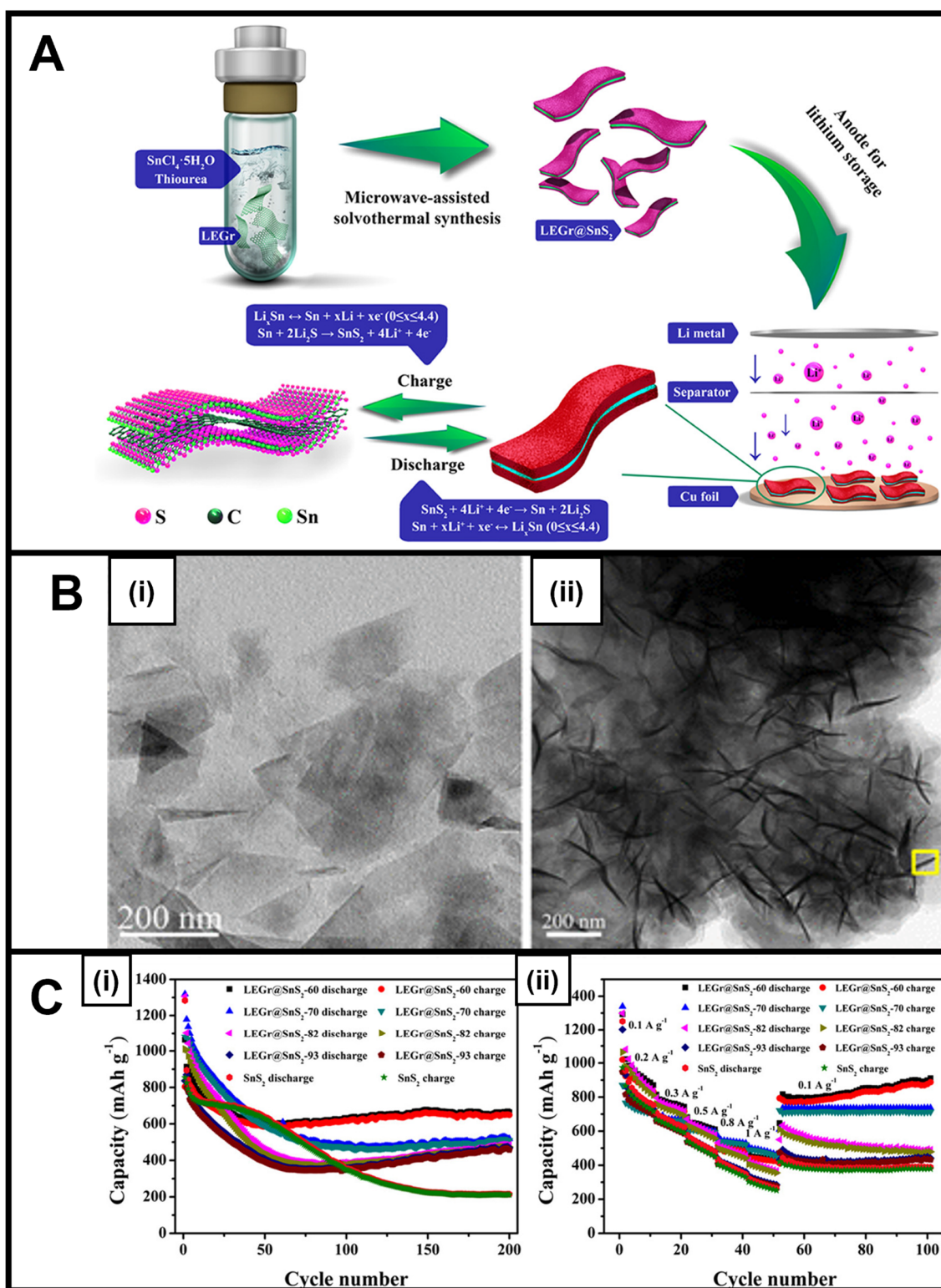


**Figure 4.** (A) Schematic of the Preparation Process and Applications of LEGr@SnS<sub>2</sub> Heterojunctions. (B) (i) TEM image of the LEGr sheets and (ii) analogous TEM image of LEGr@SnS<sub>2</sub>-60. (C) (i) Cycling performance of SnS<sub>2</sub> and LEGr@SnS<sub>2</sub>-X anodes at 300 mA g<sup>-1</sup> current density and (ii) rate performance of SnS<sub>2</sub> and LEGr@SnS<sub>2</sub>-X anodes measured at different current densities [48]. Panels (A–C) have been adapted with permission from ref. [48]. Copyright 2019 American Chemical Society.



## 5. Vanadium Sulfide

The vanadium sulfide system has historically been less well-studied and is somewhat more complex to control. Nevertheless, it can exist as either a layered or a non-layered form, depending on stoichiometric considerations. In particular, vanadium disulfide or  $\text{VS}_2$  possesses the typical TMDC layered structure, in which V is sandwiched between two S layers, and it has recently been attracting significant interest as an electrode material for energy storage applications [79]. In the process of attempting to create this material, our group was able to develop and optimize a reliable microwave-derived synthesis of a related vanadium sulfide, namely  $\text{VS}_4$ , which possesses a structural similarity to both pyrite ( $\text{FeS}_2$ ) and vaesite ( $\text{NiS}_2$ ) [80].

Interestingly,  $\text{VS}_4$  itself is highly desirable for its high theoretical capacity for both SIBs and LIBs ( $1196 \text{ mA h g}^{-1}$ ) [81]. Experimentally, it was found that patronite ( $\text{VS}_4$ ) arises in the presence of a carbon substrate due in part to the potential for favorable electron transfer, whereas in its absence,  $\text{VS}_2$  tends to form [82]. From a synthetic perspective,  $\text{VS}_4$  has been manufactured via microwave-mediated methods as 1D nanorods [18], 2D nanosheets [50,51], and 3D nanoflowers [18,51] to probe their efficacy as anodes for battery applications.

In our lab, whereas 1D nanorods were created using vanadyl acetylacetonate as the vanadium precursor and thioacetamide as the sulfur precursor within a DMF solvent after 10 min of reaction time (Figure 5A(i)), the corresponding 3D nanoflowers could be synthesized by replacing the original vanadium precursor with sodium orthovanadate and substituting DMF with aqueous solvents ranging from a water/ethanol or a pure methanol mixture. In particular,  $\text{VS}_4$  nanoflowers measuring from 100 to 200 nm in diameter were constructed by varying the solvent composition from water onwards to a water/ethanol mixture and ultimately to a water/methanol combination (Figure 5B); increasing solvent polarity led to a corresponding increase in the size of the resulting  $\text{VS}_4$  nanoflowers. Our modification to the microwave synthesis protocol was noteworthy in that the process did not require the use of a conductive carbon substrate and ran at shorter reaction times in a neutral environment while still demonstrating the capability of exerting proper compositional and morphological control [83].

A deliberate approach was used to evaluate the electrochemistry of the samples. Rather than using a planar Cu or Al foil as the current collector, a three-dimensional carbon substrate was utilized [84]. The incorporation of this substrate enabled the evaluation of the as-synthesized material over a wide voltage range with the kinetics of electron and ion transport unimpeded by the electrode design, thereby allowing for evaluation of the core material properties. The experiment was conducted, wherein the lithium electrode served as both the reference and counter electrolyte versus the transition metal sulfide functioning as the working electrode. Regarding the electrochemical testing of these samples, interestingly, unlike most conventional materials, the  $\text{VS}_4$  nanorods did not provide any evidence for the formation of a SEI layer during CV cycling during testing (Figure 5C(i)). Analogous  $\text{VS}_4$  nanorods subjected to thermal annealing even showed a greater cycling stability (Figure 5C(ii)). In the latter case, the annealing process presumably favored crystallite formation, increased the degree of crystallization overall, and diminished the presence of amorphous phases that might otherwise have led to structural disorder and a decrease in Li diffusion.

Upon the addition of MWNTs within the context of an in situ reaction, we were able to form a composite consisting of a distinctive ‘necklace’-like morphology, in which attached, evenly spaced  $\text{VS}_4$  nanorods projected radially outwards from the surface of a circular and winding spatial arrangement of an underlying MWNT backbone (Figure 5A(ii)) [18]. Electrochemical testing of this composite suggested that the addition of the MWNTs via the in situ reaction favorably enhanced both CV cycling stability and conductivity (Figure 5C(iii)). Moreover, the MWNTs themselves also could more readily accommodate for volume changes occurring during the lithiation/delithiation process. Finally, it should be noted that as compared with  $\text{VS}_4$  nanorods,  $\text{VS}_4$  nanoflowers maintained a better enhanced

reversibility during CV cycling (Figure 5C(iv)), a finding attributable most likely to an increase in surface area and porosity, which subsequently led to both an improved Li-ion transport and a greater capability to accommodate for volume change [34].

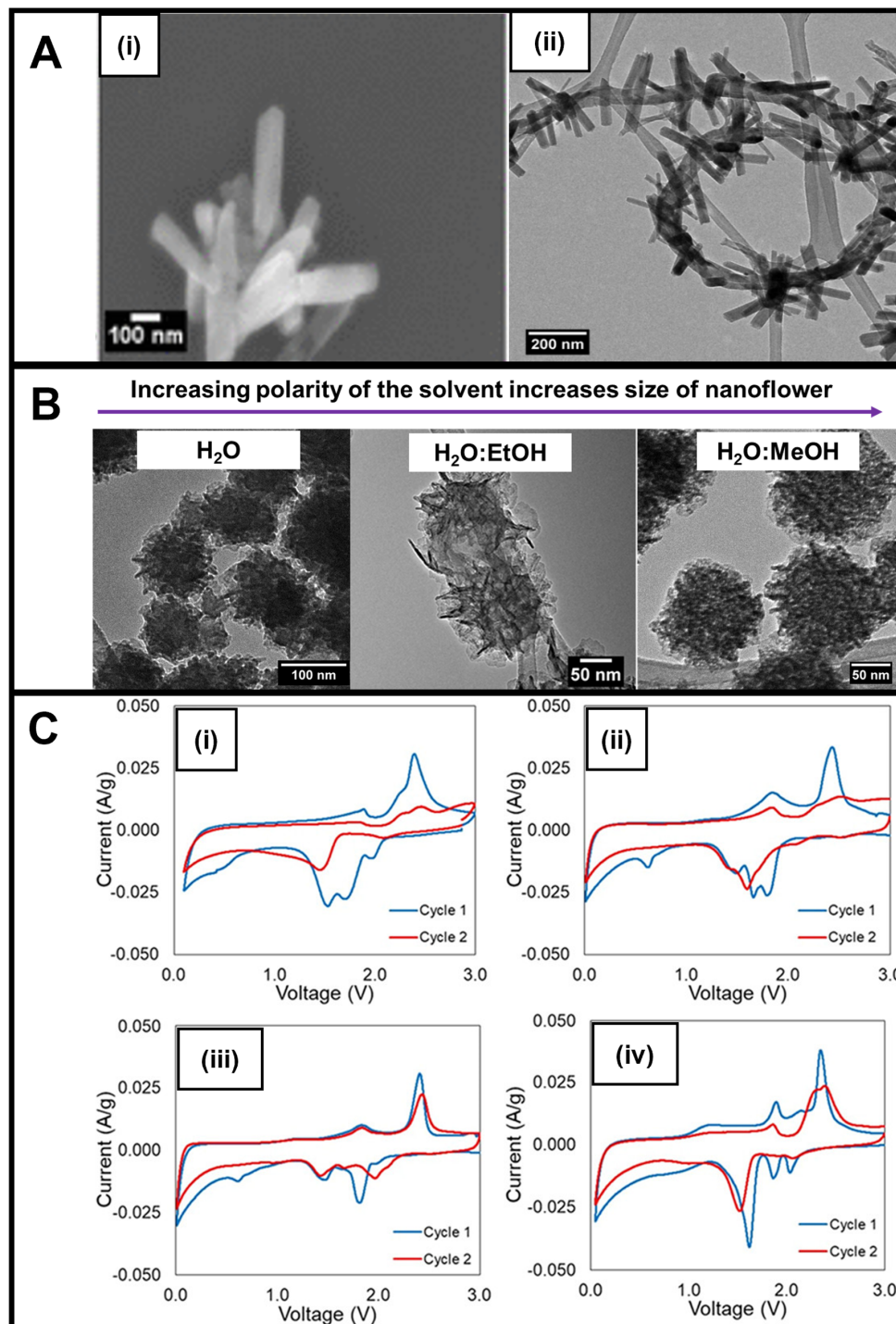


**Figure 5.** (A) (i) SEM image of as-prepared VS<sub>4</sub> nanorods and (ii) HRTEM image of as-prepared VS<sub>4</sub> nanorod/MWNT composites. (B) TEM images of VS<sub>4</sub> as 3D nanoflowers synthesized in the presence of water (NF-W), a water/ethanol mixture, and a water/methanol mixture (NF-M). (C) CVs of (i) pristine VS<sub>4</sub> nanorods, (ii) annealed VS<sub>4</sub> nanorods, (iii) annealed VS<sub>4</sub> nanorod/MWNT composites, and (iv) VS<sub>4</sub> nanoflowers [18]. These data sets were obtained at a 0.1 mV/s scan rate between 0.01–0.05 and 3.0 V versus Li/Li<sup>+</sup>. Panels (A–C) have been adapted with permission from ref. [18]. Copyright 2020 American Chemical Society.



In another study, microwave-synthesized  $\text{VS}_4$  nanosheets were grown as nanospheres, hollow nanospheres, and nanoflowers (with the precise morphology controlled by adjusting the temperature and duration of the microwave heating), and investigated for their performance as anodes in the context of sodium-ion batteries. It was found that the hollow nanospheres yielded the best performance, with a specific capacity of  $1226.7 \text{ mA h g}^{-1}$  after 100 cycles at  $200 \text{ mA g}^{-1}$ . The long-term cycling capacity was measured to be  $1129.6 \text{ mA h g}^{-1}$  after 1000 cycles at  $2 \text{ A g}^{-1}$ . This higher performance metric can likely be ascribed to the hollow nanospherical shape, which maximizes surface area-to-volume ratios while offering resistance to volume changes arising from the process of sodium-ion insertion and removal [51].

## 6. Conclusions and Outlook

Metal sulfides are attractive candidates for battery applications due to their favorable electrical conductivity, decent mechanical and thermal stability, relatively low cost, and reasonable electrochemical activity [85–87]. As such, the use of microwave-assisted reactions represents a viable, rapid, facile, and reasonably mild methodology with which to produce high-quality, pure metal sulfides in large quantities. These protocols have enabled both chemical and morphological control for the production of metal sulfides, incorporating different sizes and dimensions that are relevant for energy applications. For example, as shown in Table 1,  $\text{MoS}_2$  nanosheets,  $\text{VS}_4$  nanorods,  $\text{Fe}_3\text{S}_4$  nanosheets, and  $\text{CuS}$  flowers generated through the mediation of microwave-based chemistry have all shown important promise for battery applications.

From the prior literature, it is clear that the effect of varying dimensionality and morphology is significant, although it is difficult to draw any broad, generalizable conclusions. For example, we have found that, with  $\text{VS}_4$ , the use of 3D nanoflowers as opposed to 1D nanorods was seen to increase the observed reversibility, presumably due in part to the comparative increase in the number of exposed surface-active sites on the constituent 2D nanosheets of the ‘flower-like’ motifs [18]. By contrast, due to the increased interfacial contact between the metal sulfide and the carbon-based support,  $\text{In}_2\text{S}_3$  particle-graphene composites exhibited an enhanced electrochemical activity as compared with their  $\text{In}_2\text{S}_3$  flower-graphene analogs [44]. Moreover, other unexpected factors, such as the choice of the solution electrolyte, can influence the behavior of metal sulfides incorporated within battery systems; for example, the use of an ether-based electrolyte (as opposed to other electrolyte compositions) can optimize the overall performance and cyclability of certain metal sulfides for battery performance [41,47].

In addition, their associated carbon-based composites, composed of materials in which carbon additives were added to the underlying metal sulfide-based frameworks, such as either  $\text{In}_2\text{S}_3$ -nanoparticle-on-sheet or  $\text{VS}_4$  ‘necklace-like’ motifs, exhibited perceptibly enhanced electrochemical performance. Specifically, sulfides combined with MWNTs, graphene, and rGO yielded measurable improvements in both cyclability and capacity, implying the legitimate value of introducing conductive carbon additives as a means of increasing conductivity.

It is worth noting that the intrinsic flexibility of microwave-based techniques suggests the adaptability of this methodology towards fabricating ever more geometrically sophisticated architectures. Regarding the issue of morphological complexity, core@shell motifs are known to increase the stability and capacity of samples for LIB applications, presumably because the core–shell interface creates desirable void spaces that allow for not only the ability to account for volume changes during cycling but also the capability of facilitating electrolyte penetration. As such,  $\text{Cu@MoS}_2$  core–shell nanowires were found to possess a higher reversible capacity of  $570.6 \text{ mA h g}^{-1}$  after 250 cycles at a current density of  $0.5 \text{ A g}^{-1}$  as compared with  $\text{MoS}_2$  alone [52].

With respect to the parallel issue of enabling chemical tuning, the example of  $\text{Mo}_{1-x}\text{W}_x\text{S}_2$  alloy nanoflowers produced from microwave-assisted procedures enabled an improvement in electrochemical performance as compared with either pure  $\text{WS}_2$  or  $\text{MoS}_2$  alone.

Specifically, the initial discharge and charge capacities of the  $\text{Mo}_{0.5}\text{W}_{0.5}\text{S}_2$  alloy were 774.9 and 635.9  $\text{mA h g}^{-1}$ , with a high initial Coulombic efficiency (CE) of 82.1%; indeed, the reversible capacity of the alloy was found to increase with measured CE values of 97.0% and 99.4% for the 3rd and 100th cycles, respectively [53]. Furthermore, the  $\text{Mo}_{0.5}\text{W}_{0.5}\text{S}_2$  alloy electrode maintained a reversible capacity of 271.9  $\text{mA h g}^{-1}$  after 400 cycles. In this case, varying and optimizing the Mo/W ratio led to enhancements in both electronic conductivity and cycling stability, presumably due to the tailorability of the interlayer spacing dimension within these materials, thereby allowing for more effective Li-ion diffusion and volume accommodation.

Moreover, chemical tuning via doping of the sulfur in these materials with other chalcogenide elements using microwave-assisted synthesis procedures is also possible and can boost electrochemical performance as compared with pure sulfides. For example,  $\text{CuS}_{0.96}\text{Te}_{0.04}$  nanosheets prepared using microwave-assisted synthesis were found to exhibit excellent performance metrics as a magnesium-ion battery cathode, as these were characterized by a specific capacity of 394.5  $\text{mA h g}^{-1}$  at 50  $\text{mA g}^{-1}$  current density, as compared with that of 305.4  $\text{mA h g}^{-1}$  for pure CuS nanosheets measured under identical conditions. Furthermore, the long-term specific capacity for the  $\text{CuS}_{0.96}\text{Te}_{0.04}$  nanosheets yielded a promising 114.8  $\text{mA h g}^{-1}$  value after 200 cycles at 500  $\text{mA g}^{-1}$ . These enhancements in performance are attributed not only to an increase in Mg-ion mobility and diffusion kinetics due to the larger size and polarizability of the Te anions but also to improvements in redox reversibility behavior [54].

While all of this prior work suggests that considerable progress has been made in the investigation of binary metal sulfides for energy storage applications, further research is still necessary for sulfide materials to overcome their current inherent limitations and achieve their full potential. As such, several key issues still need to be tackled and are listed as follows:

- (1) In the realm of material science and engineering, crucial chemical strategies associated with addressing the fabrication of tailored heterostructures, doping with heteroatoms, and the directed introduction of defects and vacancies should be more fully explored.
- (2) The role of experimental reaction parameters in dictating structure–property–performance relationships that are relevant to battery performance is a fundamentally difficult challenge in assessing how the desired electrode performance can be informed and ultimately tuned by the rational selection and synthesis of target materials. Probing and optimizing microwave-assisted synthesis methods, with their potential to induce an improved control over nanomaterial composition, nucleation, growth, morphology, and other characteristics, will facilitate all of these important outcomes.
- (3) A theoretical understanding of the many factors that contribute to, for instance, electrode performance and stability, coupled with the acquisition of basic mechanistic insights, will be necessary for analyzing and perfecting charge storage behavior. Specifically, computational simulation will enable and strengthen knowledge about relevant reaction mechanisms and kinetics so as to yield greater improvements in battery safety and material optimization.
- (4) Finally, although it is beyond the scope of the current review, it is worth pointing out that a number of in situ synchrotron-based characterization techniques, such as operando XRD, ex situ XAS, and XRF, have all been successfully used to assess the simultaneous chemical and physical evolution of sulfide-based systems, including  $\text{MoS}_2$  and CuS within the context of practical, operating batteries, as a means of tracking nuanced changes in their structure, chemistry, and morphology as a function of their electrochemical performance [14,88]. In combination with other structural characterization methods which allow for the monitoring of the evolution of battery components in use, such as in situ TEM [78], these techniques have been employed and will continue to be utilized in terms of elucidating relevant electrochemical mechanisms, analyzing the composition of SEI layers, and providing valuable infor-

mation about not only possible side reactions but also key electron/ion transport pathways [86].

**Author Contributions:** K.L.S. and J.F.: contributions to the drafting, design, and data acquisition, interpretation, revision & approval, associated with the paper; C.R.T., E.S.T., A.C.M. and K.J.T.: contributions to the data acquisition, interpretation, revision & approval, associated with the paper; S.S.W.: contributions to the original conception, drafting, design, and data acquisition, interpretation, revision & approval, associated with the paper. And S.S.W. has acted as a point of contact between the editor and the other authors, keeping the co-authors informed and involving them in major decisions about the paper. All authors have read and agreed to the published version of the manuscript.

**Funding:** All of the work described in these studies was funded as part of the Center for Mesoscale Transport Properties (m2M), an Energy Frontier Research Center supported by the U.S. Department of Energy, Office of Science, Basic Energy Sciences, under award #DE-SC0012673. Experimental research characterization was carried out in part at the Center for Functional Nanomaterials, Brookhaven National Laboratory, an Office of Science User Facility, which is supported by the U.S. Department of Energy, Office of Basic Energy Sciences, under Contract No. DE-SC0012704. E.S.T. acknowledges funding from the William and Jane Knapp Chair for Energy and the Environment.

**Data Availability Statement:** Data is contained within the article itself.

**Conflicts of Interest:** The authors declare no conflict of interest.

## References

- Ahmad, M.W.; Farva, U.; Khan, M.A. Low temperature synthesis of iron pyrite ( $\text{FeS}_2$ ) nanospheres as a strong solar absorber material. *Mater. Lett.* **2018**, *228*, 129–132. [\[CrossRef\]](#)
- Liu, X.; Gao, L.; Yue, G.; Zheng, H.; Zhang, W. Efficient dye-sensitized solar cells incorporating hybrid counter electrode of  $\text{CuMnSnS}_4$  microspheres/carbon nanotubes. *Sol. Energy* **2017**, *158*, 952–959. [\[CrossRef\]](#)
- Baptayev, B.; Mustazheb, D.; Abilova, Z.; Balanay, M.P. Nanostructured flower-shaped  $\text{CuCo}_2\text{S}_4$  as a Pt-free counter-electrode for dye-sensitized solar cells. *Chem. Commun.* **2020**, *56*, 12190–12193. [\[CrossRef\]](#) [\[PubMed\]](#)
- Liu, M.; Li, G.; Chen, X. One-Pot Controlled Synthesis of Sponglike  $\text{CuInS}_2$  Microspheres for Efficient Counter Electrode with Graphene Assistance in Dye-Sensitized Solar Cells. *ACS Appl. Mater. Interfaces* **2014**, *6*, 2604–2610. [\[CrossRef\]](#)
- Liu, Y.; Li, Y.; Kang, H.; Jin, T.; Jiao, L. Design, synthesis, and energy-related applications of metal sulfides. *Mater. Horiz.* **2016**, *3*, 402–421. [\[CrossRef\]](#)
- Heift, D. Iron Sulfide Materials: Catalysts for Electrochemical Hydrogen Evolution. *Inorganics* **2019**, *7*, 75. [\[CrossRef\]](#)
- Laursen, A.B.; Kegnaes, S.; Dahl, S.; Chorkendorff, I. Molybdenum sulfides—Efficient and viable materials for electro—and photoelectrocatalytic hydrogen evolution. *Energy Environ. Sci.* **2012**, *5*, 5577–5591. [\[CrossRef\]](#)
- Li, C.; Wang, Y.; Jiang, H.; Wang, X. Biosensors Based on Advanced Sulfur-Containing Nanomaterials. *Sensors* **2020**, *20*, 3488. [\[CrossRef\]](#)
- Fei, W.; Zhang, M.; Fan, X.; Ye, Y.; Zhao, M.; Zheng, C.; Li, Y.; Zheng, X. Engineering of bioactive metal sulfide nanomaterials for cancer therapy. *J. Nanobiotechnol.* **2021**, *19*, 93. [\[CrossRef\]](#)
- Goel, S.; Chen, F.; Cai, W. Synthesis and Biomedical Applications of Copper Sulfide Nanoparticles: From Sensors to Theranostics. *Small* **2014**, *10*, 631–645. [\[CrossRef\]](#)
- Hou, C.; Wang, B.; Murugadoss, V.; Vupputuri, S.; Chao, Y.; Guo, Z.; Wang, C.; Du, W. Recent Advances in  $\text{Co}_3\text{O}_4$  as Anode Materials for High-Performance Lithium-Ion Batteries. *Eng. Sci.* **2020**, *11*, 19–30. [\[CrossRef\]](#)
- Lu, J.; Chen, Z.; Pan, F.; Cui, Y.; Amine, K. High-Performance Anode Materials for Rechargeable Lithium-Ion Batteries. *Electrochem. Energy Rev.* **2018**, *1*, 35–53. [\[CrossRef\]](#)
- Abraham, A.; Wang, L.; Quilty, C.D.; Lutz, D.M.; McCarthy, A.H.; Tang, C.R.; Dunkin, M.R.; Housel, L.M.; Takeuchi, E.S.; Marschilok, A.C.; et al. Defect Control in the Synthesis of 2 D  $\text{MoS}_2$  Nanosheets: Polysulfide Trapping in Composite Sulfur Cathodes for Li-S Batteries. *ChemSusChem* **2020**, *13*, 1517–1528. [\[CrossRef\]](#) [\[PubMed\]](#)
- Quilty, C.D.; Housel, L.M.; Bock, D.C.; Dunkin, M.R.; Wang, L.; Lutz, D.M.; Abraham, A.; Bruck, A.M.; Takeuchi, E.S.; Takeuchi, K.J.; et al. Ex Situ and Operando XRD and XAS Analysis of  $\text{MoS}_2$ : A Lithiation Study of Bulk and Nanosheet Materials. *ACS Appl. Energy Mater.* **2019**, *2*, 7635–7646. [\[CrossRef\]](#)
- Mu, Z.; Gao, S.; Huo, S.; Zhao, K. Mixed-phase 1T/2H- $\text{WS}_2$  nanosheets on N-doped multichannel carbon nanofiber as current collector-integrated electrode for potassium battery anode. *J. Colloid Interface Sci.* **2023**, *630*, 823–832. [\[CrossRef\]](#)
- Wu, Q.Y.; Abraham, A.; Wang, L.; Tong, X.; Takeuchi, E.S.; Takeuchi, K.J.; Marschilok, A.C. Electrodeposition of  $\text{MoS}_x$ : Tunable Fabrication of Sulfur Equivalent Electrodes for High Capacity or High Power. *J. Electrochem. Soc.* **2020**, *167*, 050513. [\[CrossRef\]](#)
- Xiao, Y.; Lee, S.H.; Sun, Y.-K. The Application of Metal Sulfides in Sodium Ion Batteries. *Adv. Energy Mater.* **2017**, *7*, 1601329. [\[CrossRef\]](#)

18. Salvatore, K.L.; Tan, S.; Tang, C.; Gan, J.; Licht, M.; Lin, C.-H.; Tong, X.; Chen-Wiegar, Y.-c.K.; Takeuchi, E.S.; Takeuchi, K.J.; et al. Microwave-Based Synthesis of Functional Morphological Variants and Carbon Nanotube-Based Composites of VS<sub>4</sub> for Electrochemical Applications. *ACS Sustain. Chem. Eng.* **2020**, *8*, 16397–16412. [\[CrossRef\]](#)
19. Li, X.; Wang, J. One-dimensional and two-dimensional synergized nanostructures for high-performing energy storage and conversion. *InfoMat* **2020**, *2*, 3–32. [\[CrossRef\]](#)
20. Shi, Y.; Pan, X.; Li, B.; Zhao, M.; Pang, H. Co<sub>3</sub>O<sub>4</sub> and its composites for high-performance Li-ion batteries. *Chem. Eng. J.* **2018**, *343*, 427–446. [\[CrossRef\]](#)
21. Wang, B.; Lu, X.-Y.; Wong, K.Y.; Tang, Y. Facile solvothermal synthesis and superior lithium storage capability of Co<sub>3</sub>O<sub>4</sub> nanoflowers with multi-scale dimensions. *Mater. Chem. Front.* **2017**, *1*, 468–476. [\[CrossRef\]](#)
22. Sun, H.; Ahmad, M.; Zhu, J. Morphology-controlled synthesis of Co<sub>3</sub>O<sub>4</sub> porous nanostructures for the application as lithium-ion battery electrode. *Electrochim. Acta* **2013**, *89*, 199–205. [\[CrossRef\]](#)
23. Hoa, L.T.; Chung, J.S.; Hur, S.H. A highly sensitive enzyme-free glucose sensor based on Co<sub>3</sub>O<sub>4</sub> nanoflowers and 3D graphene oxide hydrogel fabricated via hydrothermal synthesis. *Sens. Actuators B Chem.* **2016**, *223*, 76–82. [\[CrossRef\]](#)
24. Davino, S.; Callegari, D.; Pasini, D.; Thomas, M.; Nicotera, I.; Bonizzoni, S.; Mustarelli, P.; Quartarone, E. Cross-Linked Gel Electrolytes with Self-Healing Functionalities for Smart Lithium Batteries. *ACS Appl. Mater. Interfaces* **2022**, *14*, 51941–51953. [\[CrossRef\]](#)
25. Callegari, D.; Colombi, S.; Nitti, A.; Simari, C.; Nicotera, I.; Ferrara, C.; Mustarelli, P.; Pasini, D.; Quartarone, E. Autonomous Self-Healing Strategy for Stable Sodium-Ion Battery: A Case Study of Black Phosphorus Anodes. *ACS Appl. Mater. Interfaces* **2021**, *13*, 13170–13182. [\[CrossRef\]](#)
26. Li, H.; Wang, Y.; Huang, J.; Zhang, Y.; Zhao, J. Microwave-assisted Synthesis of CuS/Graphene Composite for Enhanced Lithium Storage Properties. *Electrochim. Acta* **2017**, *225*, 443–451. [\[CrossRef\]](#)
27. Wang, L.; Zhang, Y.; McBean, C.L.; Scofield, M.E.; Yin, J.; Marschilok, A.C.; Takeuchi, K.J.; Takeuchi, E.S.; Wong, S.S. Understanding the Effect of Preparative Approaches in the Formation of “Flower-like” Li<sub>4</sub>Ti<sub>5</sub>O<sub>12</sub>—Multiwalled Carbon Nanotube Composite Motifs with Performance as High-Rate Anode Materials for Li-Ion Battery Applications. *J. Electrochem. Soc.* **2017**, *164*, A524–A534. [\[CrossRef\]](#)
28. Qin, W.; Chen, T.; Pan, L.; Niu, L.; Hu, B.; Li, D.; Li, J.; Sun, Z. MoS<sub>2</sub>-reduced graphene oxide composites via microwave assisted synthesis for sodium ion battery anode with improved capacity and cycling performance. *Electrochim. Acta* **2015**, *153*, 55–61. [\[CrossRef\]](#)
29. Youn, D.H.; Jo, C.; Kim, J.Y.; Lee, J.; Lee, J.S. Ultrafast synthesis of MoS<sub>2</sub> or WS<sub>2</sub>-reduced graphene oxide composites via hybrid microwave annealing for anode materials of lithium ion batteries. *J. Power Sources* **2015**, *295*, 228–234. [\[CrossRef\]](#)
30. Li, J.; Wang, H.; Wei, W.; Meng, L. Advanced MoS<sub>2</sub> and graphene heterostructures as high-performance anode for sodium-ion batteries. *Nanotechnology* **2019**, *30*, 104003. [\[CrossRef\]](#)
31. Zhang, X.; Xiang, J.; Mu, C.; Wen, F.; Yuan, S.; Zhao, J.; Xu, D.; Su, C.; Liu, Z. SnS<sub>2</sub> Nanoflakes Anchored Graphene obtained by Liquid Phase Exfoliation and MoS<sub>2</sub> Nanosheet Composites as Lithium and Sodium Battery Anodes. *Electrochim. Acta* **2017**, *227*, 203–209. [\[CrossRef\]](#)
32. Lui, G.; Jiang, G.; Duan, A.; Broughton, J.; Zhang, J.; Fowler, M.W.; Yu, A. Synthesis and Characterization of Template-Free VS<sub>4</sub> Nanostructured Materials with Potential Application in Photocatalysis. *Ind. Eng. Chem. Res.* **2015**, *54*, 2682–2689. [\[CrossRef\]](#)
33. Zhou, Y.; Li, Y.; Yang, J.; Tian, J.; Xu, H.; Yang, J.; Fan, W. Conductive Polymer-Coated VS<sub>4</sub> Submicrospheres As Advanced Electrode Materials in Lithium-Ion Batteries. *ACS Appl. Mater. Interfaces* **2016**, *8*, 18797–18805. [\[CrossRef\]](#) [\[PubMed\]](#)
34. Yang, G.; Zhang, B.; Feng, J.; Wang, H.; Ma, M.; Huang, K.; Liu, J.; Madhavi, S.; Shen, Z.; Huang, Y. High-Crystallinity Urchin-like VS<sub>4</sub> Anode for High-Performance Lithium-Ion Storage. *ACS Appl. Mater. Interfaces* **2018**, *10*, 14727–14734. [\[CrossRef\]](#) [\[PubMed\]](#)
35. Polshettiwar, V.; Nadagouda, M.N.; Varma, R.S. Microwave-assisted chemistry. A rapid and sustainable route to synthesis of organics and nanomaterials. *Aust. J. Chem.* **2009**, *62*, 16–26. [\[CrossRef\]](#)
36. Becerra-Paniagua, D.K.; Diaz-Cruz, E.B.; Baray-Calderon, A.; Garcia-Angelmo, A.R.; Regalado-Perez, E.; Rodriguez-Torres, M.d.P.; Martinez-Alonso, C. Nanostructured metal sulphides synthesized by microwave-assisted heating: A review. *J. Mater. Sci. Mater. Electron.* **2022**, *33*, 22631–22667. [\[CrossRef\]](#)
37. Wang, Z.; Rafai, S.; Qiao, C.; Jia, J.; Zhu, Y.; Ma, X.; Cao, C. Microwave-Assisted Synthesis of CuS Hierarchical Nanosheets as the Cathode Material for High-Capacity Rechargeable Magnesium Batteries. *ACS Appl. Mater. Interfaces* **2019**, *11*, 7046–7054. [\[CrossRef\]](#) [\[PubMed\]](#)
38. Liu, R.-h.; Zhang, Y.-h.; Wang, D.-d.; Xu, L.-j.; Luo, S.-h.; Wang, Q.; Liu, X. Microwave-assisted synthesis of self-assembled camellia-like CuS superstructure of ultra-thin nanosheets and exploration of its sodium ion storage properties. *J. Electroanal. Chem.* **2021**, *898*, 115607. [\[CrossRef\]](#)
39. Wang, Y.; Zhang, Y.; Li, H.; Peng, Y.; Li, J.; Wang, J.; Hwang, B.-J.; Zhao, J. Realizing high reversible capacity: 3D intertwined CNTs inherently conductive network for CuS as an anode for lithium ion batteries. *Chem. Eng. J.* **2018**, *332*, 49–56. [\[CrossRef\]](#)
40. Yuan, D.; Huang, G.; Zhang, F.; Yin, D.; Wang, L. Facile synthesis of CuS/rGO composite with enhanced electrochemical lithium-storage properties through microwave-assisted hydrothermal method. *Electrochim. Acta* **2016**, *203*, 238–245. [\[CrossRef\]](#)
41. Li, J.; Yan, D.; Lu, T.; Qin, W.; Yao, Y.; Pan, L. Significantly Improved Sodium-Ion Storage Performance of CuS Nanosheets Anchored into Reduced Graphene Oxide with Ether-Based Electrolyte. *ACS Appl. Mater. Interfaces* **2017**, *9*, 2309–2316. [\[CrossRef\]](#) [\[PubMed\]](#)



42. Qin, W.; Li, D.; Zhang, X.; Yan, D.; Hu, B.; Pan, L. ZnS nanoparticles embedded in reduced graphene oxide as high performance anode material of sodium-ion batteries. *Electrochim. Acta* **2016**, *191*, 435–443. [\[CrossRef\]](#)
43. Zhan, G.; Lin, Z.; Xu, B.; Yang, B.; Chen, X.; Wang, X.; Yang, C.; Liu, J. Cobalt sulfide-reduced graphene oxide nanohybrid as high performance sodium ion battery anode. *J. Mater. Sci. Mater* **2017**, *28*, 13710–13715. [\[CrossRef\]](#)
44. Gu, Y.; Wang, Y. Microwave hydrothermal growth of  $\text{In}_2\text{S}_3$  interconnected nanoflowers and nanoparticles on graphene for high-performance Li-ion batteries. *RSC Adv.* **2014**, *4*, 8582–8589. [\[CrossRef\]](#)
45. Qin, W.; Chen, T.; Lu, T.; Chua, D.H.C.; Pan, L. Layered nickel sulfide-reduced graphene oxide composites synthesized via microwave-assisted method as high performance anode materials of sodium-ion batteries. *J. Power Sources* **2016**, *302*, 202–209. [\[CrossRef\]](#)
46. Tian, X.; Gao, Q.; Zhang, H.; Li, Z.; Xiao, H.; Zhang, Q.; Ma, L. Uniform small-sized  $\text{MoS}_2$  from novel solution-based microwave-assisted method with exceptional reversible lithium storage properties. *Nanoscale* **2018**, *10*, 15222–15228. [\[CrossRef\]](#)
47. Wang, L.; Abraham, A.; Lutz, D.M.; Quilty, C.D.; Takeuchi, E.S.; Takeuchi, K.J.; Marschilok, A.C. Toward Environmentally Friendly Lithium Sulfur Batteries: Probing the Role of Electrode Design in  $\text{MoS}_2$ -Containing Li-S Batteries with a Green Electrolyte. *ACS Sustain. Chem. Eng.* **2019**, *7*, 5209–5222. [\[CrossRef\]](#)
48. Li, J.; Han, S.; Zhang, C.; Wei, W.; Gu, M.; Meng, L. High-Performance and Reactivation Characteristics of High-Quality, Graphene-Supported  $\text{SnS}_2$  Heterojunctions for a Lithium-Ion Battery Anode. *ACS Appl. Mater. Interfaces* **2019**, *11*, 22314–22322. [\[CrossRef\]](#)
49. Li, J.; Yan, H.; Wei, W.; Li, X.; Meng, L. Enhanced Lithium Storage Performance of Liquid-Phase Exfoliated Graphene Supported  $\text{WS}_2$  Heterojunctions. *ChemElectroChem* **2018**, *5*, 3222–3228. [\[CrossRef\]](#)
50. Zhou, N.; Qin, W.; Wu, C.; Jia, C. Graphene-attached vanadium sulfide composite prepared via microwave-assisted hydrothermal method for high performance lithium ion batteries. *J. Alloys Compd.* **2020**, *834*, 155073. [\[CrossRef\]](#)
51. Liu, B.; Wang, L.; Zhu, Y.; Peng, H.; Du, C.; Yang, X.; Zhao, Q.; Hou, J.; Cao, C. Ammonium-Modified Synthesis of Vanadium Sulfide Nanosheet Assemblies toward High Sodium Storage. *ACS Nano* **2022**, *16*, 12900–12909. [\[CrossRef\]](#) [\[PubMed\]](#)
52. Tian, Y.; Liu, X.; Cao, X.; Zhang, D.; Xiao, S.; Li, X.; Le, Z.; Li, X.; Li, H. Microwave-assisted synthesis of 1T  $\text{MoS}_2$ /Cu nanowires with enhanced capacity and stability as anode for LIBs. *Chem. Eng. J.* **2019**, *374*, 429–436. [\[CrossRef\]](#)
53. Li, J.; Yan, H.; Wei, W.; Meng, L. Microwave-assisted mass synthesis of  $\text{Mo}_{1-x}\text{W}_x\text{S}_2$  alloy composites with a tunable lithium storage property. *Dalton Trans.* **2018**, *47*, 15148–15154. [\[CrossRef\]](#) [\[PubMed\]](#)
54. Cao, Y.; Zhu, Y.; Du, C.; Yang, X.; Xia, T.; Ma, X.; Cao, C. Anionic Te-Substitution Boosting the Reversible Redox in CuS Nanosheet Cathodes for Magnesium Storage. *ACS Nano* **2022**, *16*, 1578–1588. [\[CrossRef\]](#) [\[PubMed\]](#)
55. Kumar, A.; Kuang, Y.; Liang, Z.; Sun, X. Microwave chemistry, recent advancements, and eco-friendly microwave-assisted synthesis of nanoarchitectures and their applications: A review. *Mater. Today Nano* **2020**, *11*, 100076. [\[CrossRef\]](#)
56. Zhu, Y.-J.; Chen, F. Microwave-Assisted Preparation of Inorganic Nanostructures in Liquid Phase. *Chem. Rev.* **2014**, *114*, 6462–6555. [\[CrossRef\]](#)
57. Zhou, Y.; Yan, W.; Yu, X.; Chen, T.; Wang, S.; Zhao, W. Boron and nitrogen co-doped porous carbon for supercapacitors: A comparison between a microwave-assisted and a conventional hydrothermal process. *J. Energy Storage* **2020**, *32*, 101706. [\[CrossRef\]](#)
58. Solomon, G.; Mazzaro, R.; Morandi, V.; Concina, I.; Vomiero, A. Microwave-Assisted vs. Conventional Hydrothermal Synthesis of  $\text{MoS}_2$  Nanosheets: Application towards Hydrogen Evolution Reaction. *Crystals* **2020**, *10*, 1040. [\[CrossRef\]](#)
59. Shih, G.-H.; Liu, W.-R. A facile microwave-assisted approach to the synthesis of flower-like  $\text{ZnCo}_2\text{O}_4$  anode materials for Li-ion batteries. *RSC Adv.* **2017**, *7*, 42476–42483. [\[CrossRef\]](#)
60. Zhu, Y.; Guo, H.; Zhai, H.; Cao, C. Microwave-Assisted and Gram-Scale Synthesis of Ultrathin  $\text{SnO}_2$  Nanosheets with Enhanced Lithium Storage Properties. *ACS Appl. Mater. Interfaces* **2015**, *7*, 2745–2753. [\[CrossRef\]](#)
61. Du, C.-F.; Li, J.-R.; Huang, X.-Y. Microwave-Assisted Ionothermal Synthesis of  $\text{SnSe}_x$  Nanodots: A Facile Precursor Approach towards  $\text{SnSe}_2$  Nanodots/Graphene Nanocomposites. *RSC Adv.* **2016**, *6*, 9835–9842. [\[CrossRef\]](#)
62. Priecel, P.; Lopez-Sanchez, J.A. Advantages and Limitations of Microwave Reactors: From Chemical Synthesis to the Catalytic Valorization of Biobased Chemicals. *ACS Sustain. Chem. Eng.* **2019**, *7*, 3–21. [\[CrossRef\]](#)
63. Chen, Y.; Li, J.; Lei, Z.; Huo, Y.; Yang, L.; Zeng, S.; Ding, H.; Qin, Y.; Jie, Y.; Huang, F.; et al. Hollow CuS Nanoboxes as Li-Free Cathode for High-Rate and Long-Life Lithium Metal Batteries. *Adv. Energy Mater.* **2020**, *10*, 1903401. [\[CrossRef\]](#)
64. Liu, H.; He, Y.; Zhang, H.; Cao, K.; Wang, S.; Jiang, Y.; Jing, Q.-S.; Jiao, L. Lowering the voltage-hysteresis of CuS anode for Li-ion batteries via constructing heterostructure. *Chem. Eng. J.* **2021**, *425*, 130548. [\[CrossRef\]](#)
65. Wang, Z.; Zhu, Y.; Peng, H.; Du, C.; Ma, X.; Cao, C. Microwave-induced phase engineering of copper sulfide nanosheets for rechargeable magnesium batteries. *Electrochim. Acta* **2021**, *374*, 137965. [\[CrossRef\]](#)
66. Yang, X.; Du, C.; Zhu, Y.; Peng, H.; Liu, B.; Cao, Y.; Zhang, Y.; Ma, X.; Cao, C. Constructing defect-rich unconventional phase  $\text{Cu}_{7.2}\text{S}_4$  nanotubes via microwave-induced selective etching for ultra-stable rechargeable magnesium batteries. *Chem. Eng. J.* **2022**, *430*, 133108. [\[CrossRef\]](#)
67. Liu, H.; Zhou, W.; Zhang, Y. One-pot Solvothermal Synthesis of CuS-CNTs Hybrid as Binder-free Anode Material for Lithium Ion Batteries. *Colloids Interface Sci. Commun.* **2016**, *15*, 1–4. [\[CrossRef\]](#)
68. Xiao, S.; Li, X.; Sun, W.; Guan, B.; Wang, Y. General and facile synthesis of metal sulfide nanostructures: In situ microwave synthesis and application as binder-free cathode for Li-ion batteries. *Chem. Eng. J.* **2016**, *306*, 251–259. [\[CrossRef\]](#)



69. Sheardy, A.T.; Arvapalli, D.M.; Wei, J. Novel microwave synthesis of near-metallic copper sulfide nanodiscs with size control: Experimental and DFT studies of charge carrier density. *Nanoscale Adv.* **2020**, *2*, 1054–1058. [\[CrossRef\]](#)
70. Sridhar, V.; Park, H. Carbon nanofiber linked FeS<sub>2</sub> mesoporous nano-alloys as high capacity anodes for lithium-ion batteries and supercapacitors. *J. Alloys Compd.* **2018**, *732*, 799–805. [\[CrossRef\]](#)
71. Zhang, W.; Huang, Z.; Zhou, H.; Li, S.; Wang, C.; Li, H.; Yan, Z.; Wang, F.; Kuang, Y. Facile synthesis of ZnS nanoparticles decorated on defective CNTs with excellent performances for lithium-ion batteries anode material. *J. Alloys Compd.* **2020**, *816*, 152633. [\[CrossRef\]](#)
72. Xue, B.; Xu, F.; Wang, B.; Dong, A. Shape-controlled synthesis of  $\beta$ -In<sub>2</sub>S<sub>3</sub> nanocrystals and their lithium storage properties. *CrystEngComm* **2016**, *18*, 250–256. [\[CrossRef\]](#)
73. Henríquez, R.; Vásquez, C.; Muñoz, E.; Grez, P.; Martín, F.; Ramos-Barrado, J.R.; Dalchiele, E.A. Phase-pure iron pyrite (FeS<sub>2</sub>) micro- and nano-sized crystals synthesized by simple one-step microwave-assisted hydrothermal method. *Phys. E Low-Dimens. Syst. Nanostruct.* **2020**, *118*, 113881. [\[CrossRef\]](#)
74. Wang, D.; Wang, Q.; Wang, T. Shape controlled growth of pyrite FeS<sub>2</sub> crystallites via a polymer-assisted hydrothermal route. *CrystEngComm* **2010**, *12*, 3797–3805. [\[CrossRef\]](#)
75. Patra, C.R.; Odani, A.; Pol, V.G.; Aurbach, D.; Gedanken, A. Microwave-assisted synthesis of tin sulfide nanoflakes and their electrochemical performance as Li-inserting materials. *J. Solid State Electrochem.* **2007**, *11*, 186–194. [\[CrossRef\]](#)
76. Chen, P.; Su, Y.; Liu, H.; Wang, Y. Interconnected Tin Disulfide Nanosheets Grown on Graphene for Li-Ion Storage and Photocatalytic Applications. *ACS Appl. Mater. Interfaces* **2013**, *5*, 12073–12082. [\[CrossRef\]](#) [\[PubMed\]](#)
77. Zhang, L.; Yao, B.; Sun, C.; Shi, S.; Xu, W.; Zhao, K. Sulfur-Deficient Porous SnS<sub>2-x</sub> Microflowers as Superior Anode for Alkaline Ion Batteries. *Materials* **2020**, *13*, 443. [\[CrossRef\]](#)
78. Hwang, S.; Yao, Z.; Zhang, L.; Fu, M.; He, K.; Mai, L.; Wolverson, C.; Su, D. Multistep Lithiation of Tin Sulfide: An Investigation Using in Situ Electron Microscopy. *ACS Nano* **2018**, *12*, 3638–3645. [\[CrossRef\]](#)
79. Liu, M.; Zhao, Z.; Zhang, W.; Zheng, W. Perspective of Vanadium Disulfide: A Rising Star Finds Plenty of Room in Single and Multielectron Energy Storage. *Energy Fuels* **2022**, *36*, 13931–13955. [\[CrossRef\]](#)
80. Rout, C.S.; Kim, B.-H.; Xu, X.; Yang, J.; Jeong, H.Y.; Odkhui, D.; Park, N.; Cho, J.; Shin, H.S. Synthesis and Characterization of Patronite Form of Vanadium Sulfide on Graphitic Layer. *J. Am. Chem. Soc.* **2013**, *135*, 8720–8725. [\[CrossRef\]](#)
81. Pham, D.T.; Sambandam, B.; Kim, S.; Jo, J.; Kim, S.; Park, S.; Mathew, V.; Sun, Y.-K.; Kim, K.; Kim, J. A zero fading sodium ion battery: High compatibility microspherical patronite in ether-based electrolyte. *Energy Storage Mater.* **2019**, *19*, 270–280. [\[CrossRef\]](#)
82. Rajendran, K.; Kokulnathan, T.; Chen, S.-M.; Allen, J.A.; Viswanathan, C.; Therese, H.A. Nitrogen doped carbon nanofibers loaded with hierarchical vanadium tetrasulfide for the voltammetric detection of the non-steroidal anti-prostate cancer drug nilutamide. *Microchim. Acta* **2019**, *186*, 141. [\[CrossRef\]](#) [\[PubMed\]](#)
83. Dong, Y.; Du, X.-q.; Liang, P.; Man, X.-l. One-pot solvothermal method to fabricate 1D-VS<sub>4</sub> nanowires as anode materials for lithium ion batteries. *Inorg. Chem. Commun.* **2020**, *115*, 107883. [\[CrossRef\]](#)
84. McCarthy, A.H.; Mayilvahanan, K.; Dunkin, M.R.; King, S.T.; Quilty, C.D.; Housel, L.M.; Kuang, J.; Takeuchi, K.J.; Takeuchi, E.S.; West, A.C.; et al. Lithium vanadium oxide (Li<sub>1.1</sub>V<sub>3</sub>O<sub>8</sub>) thick porous electrodes with high rate capacity: Utilization and evolution upon extended cycling elucidated via operando energy dispersive X-ray diffraction and continuum simulation. *Phys. Chem. Chem. Phys.* **2021**, *23*, 139–150. [\[CrossRef\]](#) [\[PubMed\]](#)
85. Yang, X.; Liang, H.-J.; Yu, H.-Y.; Wang, M.-Y.; Zhao, X.-X.; Wang, X.-T.; Wu, X.-L. Recent progresses and challenges of metal sulfides as advanced anode materials in rechargeable sodium-ion batteries. *J. Phys. Mater.* **2020**, *3*, 042004/1–20. [\[CrossRef\]](#)
86. Wu, Y.; Zhang, C.; Zhao, H.; Lei, Y. Recent advances in ferromagnetic metal sulfides and selenides as anodes for sodium- and potassium-ion batteries. *J. Mater. Chem. A* **2021**, *9*, 9506–9534. [\[CrossRef\]](#)
87. Zhu, X.; Liu, D.; Zheng, D.; Wang, G.; Huang, X.; Harris, J.; Qu, D.; Qu, D. Dual carbon-protected metal sulfides and their application to sodium-ion battery anodes. *J. Mater. Chem. A* **2018**, *6*, 13294–13301. [\[CrossRef\]](#)
88. Sun, K.; Zhao, C.; Lin, C.-H.; Stavitski, E.; Williams, G.J.; Bai, J.; Dooryhee, E.; Attenkofer, K.; Thieme, J.; Chen-Wiegar, Y.-c.K.; et al. Operando Multi-modal Synchrotron Investigation for Structural and Chemical Evolution of Cupric Sulfide (CuS) Additive in Li-S battery. *Sci. Rep.* **2017**, *7*, 12976. [\[CrossRef\]](#)

**Disclaimer/Publisher's Note:** The statements, opinions and data contained in all publications are solely those of the individual author(s) and contributor(s) and not of MDPI and/or the editor(s). MDPI and/or the editor(s) disclaim responsibility for any injury to people or property resulting from any ideas, methods, instructions or products referred to in the content.